

Validation of a Numerical Model for the Analysis
of Thermal-Fluid Behavior in a Solar Concentrator Vessel

by

Juan Fernando Rodríguez Alvarado

SUBMITTED TO THE DEPARTMENT OF MECHANICAL ENGINEERING
IN PARTIAL FULFILLMENT OF THE REQUIREMENTS FOR THE
DEGREE OF

BACHELOR OF SCIENCE

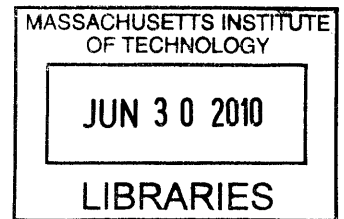
AT THE

MASSACHUSETTS INSTITUTE OF TECHNOLOGY


JUNE 2010

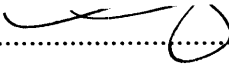
© 2010 Juan Fernando Rodríguez Alvarado
All rights reserved

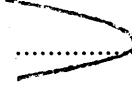
ARCHIVES



The author hereby grants to MIT permission to reproduce and to
distribute publicly paper and electronic copies of this thesis document in whole or in part
In any medium now known or hereafter created

Signature of Author:

Department of Mechanical Engineering
May 23, 2010

Certified by:

Alexander H. Slocum
Neil and Jane Pappalardo Professor of Mechanical Engineering
Thesis Supervisor

Accepted by:

John H. Lienhard V
Collins Professor of Mechanical Engineering
Chairman, Undergraduate Thesis Committee

Validation of a Numerical Model for the Analysis of Thermal-Fluid Behavior in a Solar Concentrator Vessel

by

Juan Fernando Rodríguez Alvarado

Submitted to the Department of Mechanical Engineering
on May 23, 2010 in Partial Fulfillment of the
Requirements for the Degree of Bachelor of Science in
Mechanical Engineering

Abstract

The need for innovation in the renewable energy sector is an ever-growing concern. With national-level disasters in the Gulf of Mexico, the necessity to begin the drive to develop effective and practical alternative energy sources becomes a more pressing concern. The CSPond project is an attempt to design a more simple solar thermal energy generation system that additionally addresses the intermittence issue. The CSPond system calls for a large container in which special salt mixtures are molten by solar thermal energy. The large container also acts as a thermal energy storage to address the intermittence issue that has held back the widespread application of solar energy systems.

This thesis presents a validation analysis of a numerical simulation of a molten salt system. The simulation is part of a larger design effort to develop a viable solar thermal energy option which incorporates short to medium-term thermal storage.

To validate the numerical model, a scaled version of the proposed solar vessel was used in the solar simulator built by Professor Slocum's PERG to simulate normal operation procedures. This data was then compared to the numerical simulations.

This comparison found that the numerical simulation does not capture the dynamics of the temperature rise in the system, but that it does capture the Rayleigh-Taylor instabilities, characteristic of convection.

Solutions to the issues identified above are proposed and analyzed. These include the consideration of several modes of thermal interactions with the environment, the optical interactions between the solar beam and the molten salt medium, modifying the boundary conditions and finally, including the temperature of all relevant thermophysical properties to better capture the convective behavior of the molten salt system.

Thesis Supervisor: Alexander H. Slocum

Title: Neil and Jane Pappalardo Professor of Mechanical Engineering

Acknowledgements

I would like to acknowledge the following people on providing help and advice for this thesis: Barbara Hughey for her huge help with MathCAD; to JC Nave for providing the model which became the focus of this thesis and his help with the coding and data processing for this thesis. Daniel Codd for his help in learning to use the solar simulator safely and continuously checking up on my progress even though he wasn't in charge of me. Thomas McKrell for the safety training that allowed me to start my experiments. To Professor Slocum for his support and humor this last semester. To Lisa Tacoronte and Yelena Bagdasarova for their humor, their company and their general craziness during the final push on finishing this thing, and to Lucy Ramírez for her cheering me on all the way from Mexico.

Table of Contents

Nomenclature	8
Chapter 1 Introduction	10
1.1 The CSPond Project.....	11
1.2 Governing Equations of a Thermal-Fluid System.....	12
1.2.1 The Navier-Stokes Equations	12
1.2.2 The Heat Equation	13
1.2.3 Assumed Boundary Conditions.....	14
1.2.3.1 System Boundaries.....	14
1.2.4 Molten Salt Properties	14
1.3 Modeling the Solar Input.....	14
1.3.1 The Planck Model	15
1.3.3 The Reference Solar Spectral Irradiance	15
1.3.3.1 Absolute Air Mass.....	17
1.3.3.2 Angstrom Turbidity.....	18
1.3.3.3 Column Water Vapor Equivalent	18
1.3.3.4 Column Ozone Equivalent.....	19
1.3.4 The Solar Energy Input as a Volumetric Heat Source.....	19
1.3.5 Optical System Assumptions [2].....	21
1.4 The Projection Method	21
Chapter 2 The Solar Simulator	24
2.1 The Simulator Light Source	24
2.2 Operation of the Solar Simulator	25
Chapter 3 Setup & Procedure	26
3.1 Experiment Design.....	26
3.1.1 Receiver Tank Geometry.....	26

3.2 Experimental Procedure	26
3.2.1 Sensor Setup	27
3.2.2 Experimental Protocol.....	28
3.3 Simulation Parameters	29
3.4 The Rayleigh Number	30
3.4.1 The Aspect Ratio	31
Chapter 4 Experimental Results.....	32
4.1 Onset of Convection and the Rayleigh Number	32
4.2 Dimensionless Rise Time	33
4.3 Non-Dimensional Steady State Temperature.....	35
Chapter 5 Simulation Results	37
5.1 Temperature Rise Dynamics.....	37
5.2 Identification of Convective Behavior	37
5.3 The Rayleigh Number in the Simulations	39
Chapter 6 Discussion & Conclusions	41
6.1 Validity of the Boundary Condition Assumptions	41
6.1.1 The adiabatic free-surface assumption	41
6.1.2 Geometric assumptions.....	41
6.2 Validity of the Material Property Assumptions	42
6.2.1 Optical Absorbance Model.....	42
6.2.2 Constant Thermophysical Properties.....	42
6.3 Conclusion	43
Bibliography.....	44

List of Figures

Figure 1: Planck model and NREL solar data.....	16
---	----

Figure 2: Definition of the solar zenith angle	18
Figure 3: Volumetric heat generation models	20
Figure 4: The Projection Method.....	23
Figure 5: Solar simulator in with salt heat exchanger in operation	25
Figure 6: Schematic of the receiver tank geometry.....	26
Figure 7: Sensor setup	27
Figure 8. Salt receiver tank with insulation	29
Figure 9: Experimental Rayleigh numbers	33
Figure 10. Dimensionless time constant as a function of aspect ratio.....	34
Figure 11: Dimensionless steady state temperature at vessel bottom.....	35
Figure 12: Dimensionless steady state temperature at the salt free surface	36
Figure 13: Time history of the average vessel temperature	37
Figure 14: Cross-section of the simulated time evolution with aspect ratio $\phi = 0.150$	38
Figure 15: Simulated three-dimensional isothermal surfaces with aspect ratio $\phi = 0.150$	39
Figure 16. Rayleigh numbers in the numerical simulation.....	40
Figure 17: Light attenuation coefficient in the wavelength absorption range	48
Figure 18: Graphical form of the critical Rayleigh number for cylindrical geometry	49
Figure 19: Solar receiver geometry for thermal losses in the radial direction	52

List of Tables

Table 1: Functional requirements and corresponding design parameters for the solar simulator.....	24
Table 2: Simulation parameters.....	30
Table 3: Critical Rayleigh numbers for the tested aspect ratios	32

Table 4: Fit constants for the volumetric heat generation model.....	45
Table 5: Manufacturer data for the Hitec Solar Salt mixture.....	47
Table 6 Fit constants for the light attenuation coefficient.....	48

List of Appendixes

Appendix A: Estimating the Volumetric Heat Generation.....	45
Appendix B: Buckingham Pi Theory Analysis	46
Appendix C: Material & Optical Properties for $\text{KNO}_3\text{-NaNO}_3$ Mixtures.....	47
Appendix D: The Critical Rayleigh Number	49
Appendix E: Matlab Code	50
Appendix F: Thermal Losses	52

Nomenclature

Roman

A	area
c	speed of light in a vacuum
g	gravity
h	Planck's constant
k	thermal conductivity
k_B	Boltzmann's constant
L	height of solar receiver
L_c	critical length
m_{air}	air mass
\mathcal{P}	perimeter
q	volumetric heat generation
\bar{q}	average incoming heat flux
q_{beam}	total incoming heat flux
r	vessel radius
t	time
u	fluid velocity
C	specific heat capacity
I	spectral irradiance
Q	heat transfer
T	temperature
\bar{T}	average temperature
Z	zenith angle

Greek

α	absorption of light
α_D	thermal diffusivity
β	volumetric thermal expansion
δ	molten salt depth
λ	wavelength of incident light
μ	dynamic viscosity
ν	kinematic viscosity
ρ	density
Δ	difference

Subscripts, Superscripts and Operators

∇	del operator
\cdot	dot product
∞	environmental condition
$*$	intermediate value
m	index number
t	time derivative

A mis padres, porque por ellos he podido llegar tan lejos.

Chapter 1

Introduction

Renewable energy has become a very competitive industry, where talk of innovation and progress are constant news. Unfortunately, the United States has fallen far behind in its drive to develop renewable energy technologies. Recently, there has been a large push to expand the country's wind energy production. However, most of this capacity growth is not built by American companies, the leading companies in the wind industry are not American, they come from countries like Denmark and Spain. These countries have become leaders in the wind and solar industry, respectively.

This worrying trend is not exclusive to the renewable wind sector. Countries in the European Union have made great strides in advancing their technology development, manufacturing capabilities, and upgrading their renewable energy production capacity in the field of solar power generation. Countries like Germany and Spain have become leaders in solar power applications with Germany being a leader in the manufacture of solar panels and Spain fostering a large initiative to construct solar concentrating towers. China has also recently begun to dramatically increase its investments in the renewable energy sector, hoping to quickly become a world leader in the renewable industry.

The necessity then is not only to develop technologies for the sake of advancing technology, but to maintain the technologic and economic leadership that the United States developed for the last fifty years.

The CSPond (Concentrated Solar Power On Demand) project is thus an attempt to innovate in the field of renewable energy and simultaneously create an opportunity for the United States to begin an earnest push towards developing and adopting novel, efficient, and renewable energy technologies. It incorporates design ideas and operating principles from structures such as solar concentrating towers, yet its design forgoes the complications of building, maintaining, and operating such structures. Instead, the CSPond strives for simplicity in design and operation. These design principles have allowed the project to progress quickly, and if successful, its simplicity will drive it to become a staple in the solar thermal renewable sector.

The purpose of this thesis is to validate a thermal-fluids model through testing of the thermal-fluids behavior of molten salt mixtures in a solar simulator (See Section 2.1).

This model was used to explore the thermal-fluids behavior of a molten salt system, an integral part of the CSPond design. The simulation will be used as a design tool to explore the effects of geometry and other design factors on the performance of the solar thermal system.

1.1 The CSPond Project

The (CSPond) system builds upon existing concentrating solar power technologies while incorporating simplifying design philosophies. Many current designs of solar thermal systems employ tall tower receivers and make use of flat terrain. The current design is simplified by incorporating a solar receiver that lies near the ground. This is in contrast to building large towers, whose construction and maintenance pose higher technical, maintenance challenges, along with the possibility for higher capital risk. The CSPond design minimizes the pumping requirements that are encountered by solar towers and makes use of hillside terrain to “beam down” solar energy into a molten salt receiver.

The design of the CSPond receiver is innovative in that it not only provides a molten-salt medium for volumetric heating, but in that the molten-salt also acts as a high-capacity thermal storage system. One of the main arguments against renewable sources (solar, photovoltaic, wind) is that their current design does not immediately address the intermittence problem. The CSPond system, with a well-insulated receiver tank, is not only designed to capture solar energy but also as a mode of thermal energy storage. An insulated plate provides a thermal resistance barrier between the thermally stratified hot and cold salt layers. This design provides a continuous high quality heat source to address the intermittence problem [1].

As an example of an initial estimate for a 4 MWe CSPond system would need 2500 m³ of nitrate salt to continuously (all day, with 7 hours sunshine, 17 hours storage) drive a steam turbine generator [1]. To meet these design requirements, the solar receiver would have a depth of 5 meters and a diameter of about 25 meters. This would give the system an aspect ratio (defined in Chap. 3) of $\phi = 0.2$. The behavior of this and other systems with varying geometry were explored in this thesis.

The design of the CSPond system thus fills a critical need in solar power, in that it proposes a solution to the intermittence problem with its inherent design for thermal storage. This is critical in the solar power industry if a specific solar energy system design

will satisfy baseload needs [1]. Overcoming this technical hurdle is crucial for the growth of solar thermal industry, and the CSPond is a technological leap in the positive direction. The CSPond system then provides a continuous power source without resorting to nonrenewable sources or expensive battery-based energy storage systems to solve the intermittence problem, offering the capability for a substantial installed capacity for utilities, providing a renewable and practical source of solar thermal energy [1]. Additionally, it has the possibility to change the perceived feasibility of solar thermal, and renewables sources, as the CSPond provides an practical and realizable proposal in answering the intermittence problem. The following sections will focus on explaining the theory behind the solar thermal receiver, along with a few explanations and definitions of important parameters used to model the system.

1.2 Governing Equations of a Thermal-Fluid System

1.2.1 The Navier-Stokes Equations

The thorough analysis of the behavior of the molten salt system requires examining several key aspects of the system, including fluid dynamics, heat transfer, optics, and boundary conditions. An important component of the system is the fluid behavior of the salt as it experiences changes in its local density. These changes in local density are one of the driving mechanisms that create convection currents. Thus, it is critical to use a model which can predict the fluid motion, and simultaneously including the contributions from density changes in the fluid system. For the thermal-fluids simulations considered in this analysis, the molten salt mixtures are modeled by the incompressible Navier-Stokes (NS) equations, as presented below in Equations (1a) and (1b):

$$\vec{u}_t + (\vec{u} \cdot \nabla) \vec{u} = -\frac{1}{\rho} \nabla P + \frac{1}{\rho} \nabla \cdot \mu (\nabla \vec{u} + \nabla^\perp \vec{u}) + \vec{g} \quad (1a),$$

$$\nabla \cdot \vec{u} = 0 \quad (1b).$$

The NS equations model the behavior of a flowing, viscous liquid. Although they might appear cumbersome at first, they are simply a form of Newton's Second Law for a moving fluid. The set of equations contain a set of four unknowns: The three-dimensional

velocity vector, which makes up three unknowns, and the pressure distribution throughout the fluid system. The three equations given by Equations (1a) are complemented by a fourth, Equation (1b), the continuity equation.

1.2.2 The Heat Equation

The heat transfer mechanisms within the molten salt system are crucial to determining the performance of the CSPond system. Many important design decisions can be made by the information given by the a thermal-fluids model. The information produced by such a model will influence the design methods for extracting thermal energy from the molten salt system. A good thermal-fluids model should be able to predict the distribution of thermal energy through the entire molten salt receiver system, allowing design engineers to optimize the geometry of the receiver itself to maintain certain thermal energy distributions or to encourage certain fluid behaviors to optimize the extraction of the thermal energy from the molten salt. The thermal behavior of the molten salt is thus best represented with a the heat equation with an additional term for modeling volumetric heat source generation, which will be discussed in Section 1.3. The form of the heat equation, as used in the simulations, is presented below in Equation (2):

$$T_t + \vec{u} \cdot \nabla T = \frac{1}{\rho C} (\nabla \cdot k \nabla T + q) \quad (2).$$

As defined above, Equation (2) is a description of the time-dependent temperature behavior of the molten salt system. However, the heat equation does not only model the time-dependent temperature behavior, but also determines the temperature as a function of space, thus describing the distribution of the thermal energy in of the molten salt system, highlighting its importance, as discussed above. Equation (2) is coupled to the NS equations through two parameters, the fluid velocity, and the temperature-dependent density.

This system of equations was used to model the temperature distribution throughout the molten salt system. These equations represent a coupled thermal-fluids system, where the local temperature and fluid velocity are influenced by the local density variations, a consequence of the incident light on the molten salt receiver.

1.2.3 Assumed Boundary Conditions

1.2.3.1 System Boundaries

The system of differential equations represented by Equations (1-2) requires a set of boundary conditions to be solved for a given situation. The molten salt system makes use of several common assumptions that are made in the analysis of thermal-fluid systems. The salt vessel walls are cubical in shape and adiabatic on all sides, except for the free surface [2]. The bottom surface is reflective and is modeled as a heat source at the bottom of the vessel. Its reflective behavior is explained by Equation (20) in Appendix A.

The numerical simulation assumes a no-slip condition at the boundaries between the fluid and the containment vessel. The physical molten salt system is modeled as a viscous fluid with a finite viscosity and the shear stress is nonzero at the salt-vessel interface. This creates a vanishing local velocity at the salt-vessel interface. The free surface is modeled with a free-shear boundary condition [2], where the shear stress is set to zero and the local velocity takes a nonzero value.

1.2.4 Molten Salt Properties

The numerical simulation considers the case where the molten salt density is a function of space [2]. All other material properties (thermal conductivity, viscosity, specific heat) are held constant throughout the fluid system [2].

The space-dependent density is a necessary assumption to model the convective behavior of the molten salt system. Convective heat transfer is driven by buoyancy forces, themselves a consequence of the temperature-dependent density [3]. These systems additionally require the presence of a gravity field. Density correlations for binary salt systems, and other temperature-temperature dependent have been published [4]. The relevant data for the $\text{KNO}_3\text{-NaNO}_3$ salt mixture used in the experiments for this work are available in Appendix C.

1.3 Modeling the Solar Input

Several spectral irradiance models were considered to model the incoming solar radiation. The first simulations utilizing the current numerical simulations [2] approximated the solar irradiance with Planck's Law. The current study focuses on

utilizing empirical data obtained from the National Renewable Energy Research Laboratory (NREL). This data was used to develop a volumetric absorption model which was then used as the heat generation term q in Equation (2). Details on the derivation of the volumetric heating term as a function of molten salt depth are given in Appendix A.

1.3.1 The Planck Model

The dependence of the spectral irradiance of a blackbody at a temperature T on the wavelength λ was first described in 1901 by Max Planck [5]. This model revolutionized the scientific thought of the times [5], ushering in the revolutionary thinking that created the fields of quantum mechanics and Einstein's investigation of the photoelectric effect. The relation between spectral irradiance, temperature and wavelength is given by Equation (3) below [2]:

$$I(\lambda, T) = \frac{2hc^2}{\lambda^5} \frac{1}{e^{\frac{hc}{\lambda k_B T}} - 1} \quad (3).$$

Preliminary simulations by Nave [2] assumed that the solar spectrum could be approximated by the theoretical blackbody radiating at $T=5260$ K. However, a more accurate solar spectrum is available from NREL [6], and it is very easily integrated into the numerical model. These empirical solar spectra will be discussed in the following section.

1.3.3 The Reference Solar Spectral Irradiance

The solar industry has developed two standard spectral irradiance models (ASTM G173) in conjunction with the American Society for Testing and Materials (ASTM) and other government laboratories. These two models define a standard direct normal irradiance and a standard total (global, hemispherical, 2π steradian field of view of the standard tilted plane) spectral irradiance. The direct normal spectrum is the direct spectral component contributing to the total hemispherical spectrum [6]. The spectra, as published by NREL are shown alongside the Planck spectra in Figure (1) below:

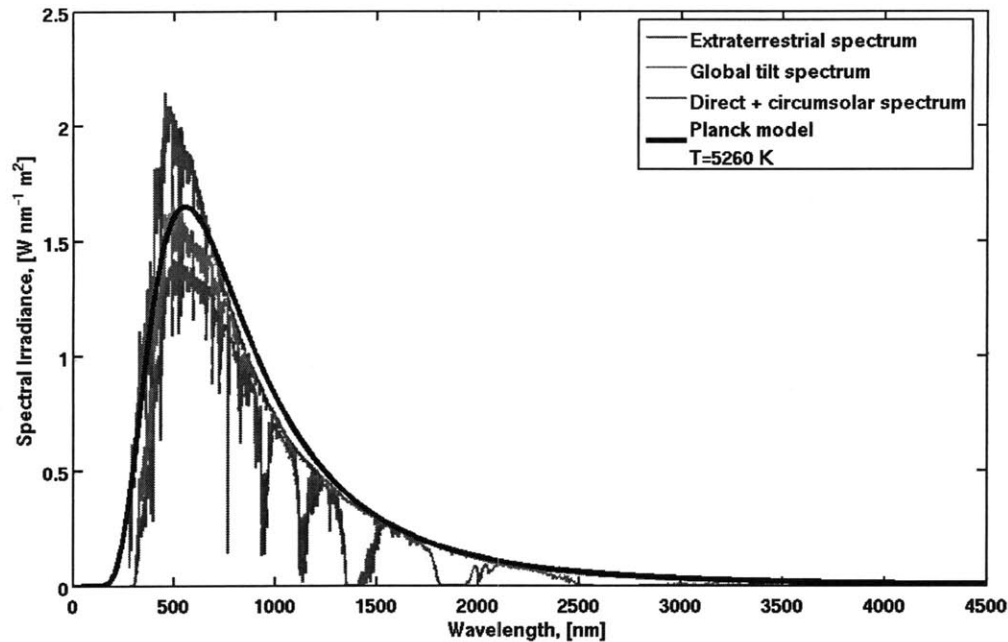


Figure 1: Planck model and NREL solar data. The NREL data for three different atmospheric conditions are compared to the Planck spectral irradiance model. The model and the Planck spectra match qualitatively, and as can be seen in Appendix A, the Planck spectra is a good quantitative estimate of the solar spectra. The extraterrestrial spectrum corresponds to the spectral irradiance as observed outside the Earth's atmosphere. The global tilt spectrum and the direct and circumsolar spectra represent two special cases, in which a theoretical reflector is subject to "average" solar conditions in the contiguous United States. The specific details of the NREL spectra are discussed below.

The ASTM G173 spectra model the terrestrial solar spectral irradiance on a surface of specified orientation under a given set of specified atmospheric conditions, outlined below [6]:

1. The 1976 U.S. Standard Atmosphere with temperature, pressure, aerosol density (rural aerosol loading), air density, molecular species density specified in 33 layers.
2. An absolute air mass of 1.5 (solar zenith angle 48.19°).
3. Angstrom turbidity (base e) at 500 nm of 0.084.
4. Total column water vapor equivalent of 1.42 cm.
5. Total column ozone equivalent of 0.34 cm.
6. Surface spectral albedo (reflectivity) of Light Soil as documented in the Jet Propulsion Laboratory.

These standard solar irradiance data are published by the NREL (an abridged version of the standard) [6] and the ASTM (the complete standard) in units of $\text{Wm}^{-2}\text{nm}^{-1}$ as a function of wavelength provide a single common reference for evaluating solar energy systems with respect to their performance measured under varying natural and artificial sources of light, (e.g. the Solar Simulator, see Chapter 2) with a range of differing spectral distributions. The conditions selected for the spectral irradiance standards are considered to be a reasonable average for the 48 US contiguous states the over a period of one year. The tilt angle approximates the average latitude of the contiguous 48 states of the United States [6].

The standard receiving surface is defined as an inclined plane at 37° tilt toward the equator, facing the Sun (i.e., the surface normal points to the Sun, at an elevation of 41.81° above the horizon) [6].

Several environmental characteristics serve to affect the extraterrestrial spectra by means of atmospheric attenuation. This phenomena is what causes the global tilt and direct & circumsolar spectra in Figure (1) to be diminished in magnitude when compared to the extraterrestrial spectrum. The environmental characteristics contributing to atmospheric attenuation are discussed in the following section.

1.3.3.1 Absolute Air Mass

The degree of attenuation of the solar radiation is a function of the atmospheric path length and the optical characteristics of the medium involved [7]. The airmass is defined as the relative path length of a direct solar beam radiance through the atmosphere [8]. An airmass of $m=1.0$ is defined to be the path travelled by a beam of sunlight when the sun is directly above a sea level location [8]. The airmass is thus a function of the zenith angle Z , and can be determined by Equation (4) below [8]:

$$m_{air} = \frac{1}{\left[\cos(Z) + 0.50572 \cdot (96.07995 - Z)^{-1.6364} \right]} \quad (4).$$

The air mass can also be estimated, without accounting for the curvature of the Earth using the approximation as given by Equation (5) below [7]:

$$m_{air} = \frac{1}{\cos(Z)} \quad (5).$$

This air mass model as given by Equation (4) is used by NREL to determine the absolute air mass value used in the Reference Solar Spectra. However, other literature recommends Equation (5) as a quick estimate for the airmass. An illustration of the definition of the zenith angle for use in Equations (4) and (5) is given by Figure (2) below:

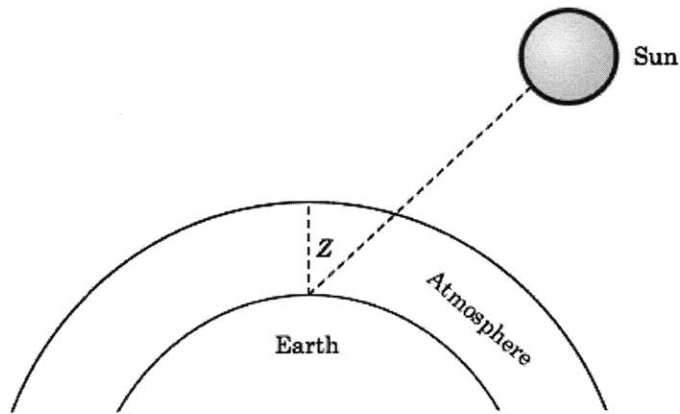


Figure 2: Definition of the solar zenith angle.

1.3.3.2 Angstrom Turbidity

The angstrom turbidity is defined as an exponent is used to quantify the effect of suspended aerosols in the atmosphere. The aerosol optical depth is the approximate quantity of aerosols that a beam must pass through as it travels through the atmosphere, relative to the standard quantity of aerosols that light must travel (in a vertical path, $m_{air} = 1.5$) through in a clean and dry atmosphere at sea level [8].

1.3.3.3 Column Water Vapor Equivalent

Water vapor in the atmosphere is the most important greenhouse gas, affecting the heat transfer interactions between the atmosphere and incoming solar energy by absorbing bands of solar radiation in the infrared range [7, 9]. The column water vapor equivalent is

defined as the equivalent amount of water produced in an air column (unit area) if it were all to condense at once.

1.3.3.4 Column Ozone Equivalent

The ozone content in the atmosphere contributes in absorbing certain wavelengths of the incoming solar radiation. Ozone absorbs waves of longer wavelength, usually in the ultraviolet range [7]. The effect of the ozone content in the upper atmosphere (15-40 km) is quantified by the column ozone equivalent, which, much like the column water equivalent, is published with the dimensions of length.

1.3.3.5 Surface Spectral Albedo

The surface spectral albedo is defined as the fraction of the incoming solar radiation that is reflected [8]. The solar energy industry usually defines albedo as a fraction of the solar radiation that is reflected from the entire surface of the air [8]. The second definition, used by astronomers and meteorologists includes the reflectance of the atmosphere, including air and cloud masses [8]. The data as reported in the NREL Standard Spectral Irradiance is for Light Soil, thus it is given under the solar industry definition.

1.3.4 The Solar Energy Input as a Volumetric Heat Source

The solar input is modeled as a volumetric heat source. From conservation of energy, the solar heat input can be modeled as function of the pond depth, as given by Equation (6):

$$q(z) = \int_0^{\infty} \alpha(\lambda) \cdot \bar{q}(\lambda, z=0) e^{-\alpha(\lambda)z} d\lambda \quad (6).$$

The first term in the right-hand side of Equation (6) represents the attenuation coefficient, which is a function of wavelength. Each material has a characteristic attenuation behavior. The attenuation coefficient then represents the ease through which a beam of light can penetrate into a medium [10]. The second term in Equation (6) represents the volumetric heat source, itself also a function of wavelength. The volumetric heat source is represented as an initial value at the molten salt free surface. The last term in the

integral in Equation (6) represents the exponential decay in the magnitude of the intensity of light as its path length through a medium increases.

This exponentially-decaying behavior is characterized by the Beer-Lambert law, which expresses that the transmission of light through a substance is a logarithmic function of the material absorption and the length of the optical path it travels through the substance [10]. The volumetric heat source, a direct result of radiation traveling through the salt mixture also obeys this law.

The average incoming heat flux (heat transfer per unit area) term as seen in Equation (6) is defined as:

$$\bar{q}(\lambda, z = 0) = q_{beam} \frac{I(\lambda, T)}{\int_0^{\infty} I(\lambda, T) d\lambda} \quad (7).$$

Equation (7) describes the form of the volumetric heat source at the surface, which will then be absorbed by the salt, and includes contributions from all incoming wavelengths. The volumetric heat generation models, as given by Equation (6) are illustrated in Figure (3) below

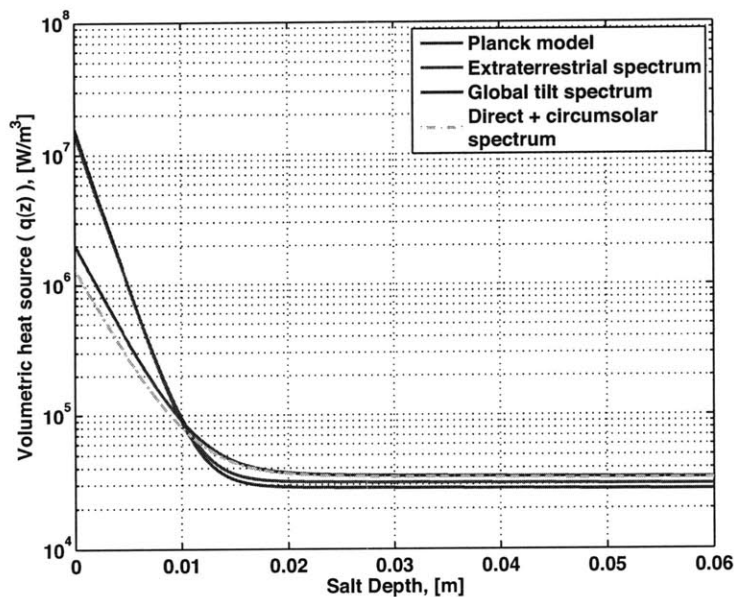


Figure 3: Volumetric heat generation models. The models shown are for the four different models considered.

The absorption coefficient is a material property and a function of the wavelength of the incident light that travels through the material. The absorption coefficient for a salt mixture was experimentally measured as a function of wavelength in a separate investigation [11]. The data for these experiments was processed using MATLAB's `cftool` utility. The fit data are available in Appendix C.

1.3.5 Optical System Assumptions [2]

The incoming solar beam was modeled as a volumetric heat source, however, it still retains some optical properties. First, the incoming beam impinges the free salt surface perpendicularly and it is completely absorbed (no reflection). Next, the entire salt surface is uniformly lit. The adiabatic walls of the simulated receiver are also reflective, with all the beam energy reflected back into the molten salt. Additionally, the scattering within the salt is reflected by the sides of the pond. Finally, the unabsorbed heat flux that reaches the bottom is completely radiated to the salt, in a mechanism explained Appendix A.

1.4 The Projection Method

The projection method is a finite difference method first published by A. J. Chorin in 1968. This method is used to solve the incompressible NS equations [12]. It provides a guiding framework to solve the NS equations in this analysis, but facilitates the solution to the coupled system as defined in Section 1.2.1.

This method provides a means to examine the the local fluid velocity and local fluid pressure independently. The projection method makes use of Equations (1-2), and the additional equations needed to describe the coupled system are represented by Equations (9-12) below.

Equation (9) represents the estimation of the local fluid velocity. It does not include the contributions to the local velocity due to the pressure gradient in the fluid:

$$\frac{u^* - u^m}{\Delta t} = -(u \cdot \nabla u)^m + \frac{\mu}{\rho} (\nabla^2 u^m) + \bar{g} \quad (9).$$

Equation (10), is used to calculate a local pressure value using the estimated local velocity:

$$\nabla \left(\frac{1}{\rho} \nabla P \right) = \frac{1}{\Delta t} \nabla u^* \quad (10).$$

The next equation, Equation (11), is used to calculate the local fluid velocity for the next time step, and it includes the contributions of the local fluid density and the pressure gradient in the fluid:

$$\frac{u^{m+1} - u^*}{\Delta t} + \frac{1}{\rho^m} \nabla P = 0 \quad (11).$$

The following equations are used to couple the fluid system to the thermal system modeled by Equation (4). The temperature distribution throughout the fluid can then be described by the heat equation as given by Equation (12):

$$\frac{T^{m+1} - T^m}{\Delta t} = - (u^m \nabla T^m) + \frac{1}{\rho^m C} (\nabla \cdot k \nabla T^m + q) \quad (12).$$

As the local density is modeled as a function of temperature, the new local temperature is used to determine the value of the fluid density by using an empirical density constitutive relation or the Boussinesq approximation [3][13]. A graphical summary of the projection method is shown by Figure (4) below:

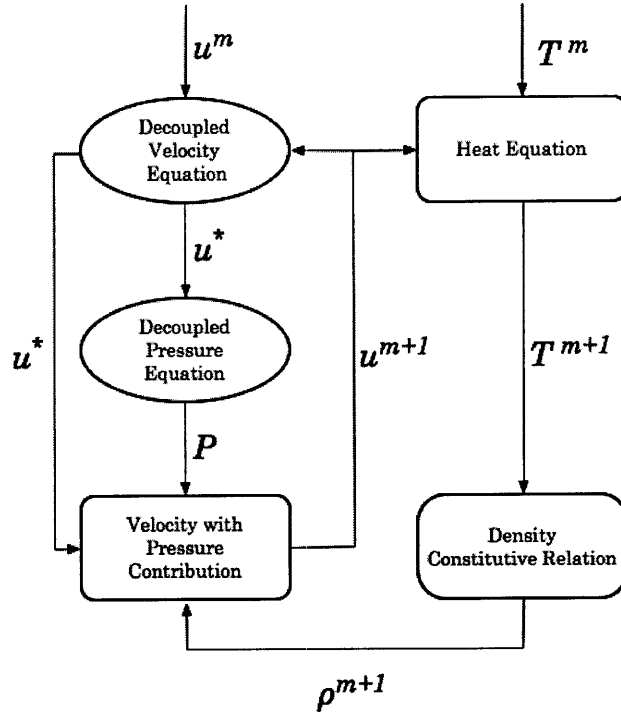


Figure 4: The Projection Method. In its first step, the projection method takes a previous velocity, u^m , to calculate an intermediate value, u^* , of the local fluid velocity by decoupling it from its pressure dependence. This value of velocity is then used to estimate the local pressure, P , values. The estimated local pressure and velocity are then used to calculate the actual velocity value, u^{m+1} , for the next time step. These velocity values can then be used to calculate the local temperature, T , by using the heat equation. This local temperature is then used to calculate a new value of the local density, ρ^{m+1} . The cycle continues until the simulation is halted by the user.

Chapter 2

The Solar Simulator

The solar simulator was built by members of the Precision Engineering Research Group for the purpose of studying solar thermal systems, along with CSPond design alternatives. The simulator followed a simplified design paradigm, using off-the-shelf components to construct an adjustable and reliable testing platform. The functional requirements and their corresponding design specifications are listed in Table (1) below [14]:

Table 1 [14]: Functional requirements and corresponding design parameters for the solar simulator. The proposed design needed to maximize simplicity and availability of the necessary components.

Functional Requirement	Design Parameter	Specification
Heat	Peak output intensity	$\geq 50 \text{ kW/m}^2$
Large output area	Diameter of output aperture	$d \geq 0.20 \text{ m}$
Adjustable height (accommodate different receivers)	Aperture height adjustability	$0 \leq h \leq 1 \text{ m}$
Adjustable tilt angle	Aperture rotation angle	$0^\circ \leq \theta \leq 90^\circ$
Low cost	Final cost	$< \$10\text{k USD}$

2.1 The Simulator Light Source

The solar simulator utilizes seven metal halide outdoor stadium lights. Industrial solar simulators utilize xenon lamps. However, following a design paradigm that called for a simplified design, metal halide lamps were chosen because of their low cost and wide availability. In normal operating conditions the seven-lamp array delivers an average of 45 kW/m^2 at the simulator aperture [14]. This value is equivalent to 33 solar equivalents

focused on the simulator aperture as calculated using the NREL solar constant of 1366.1 W/m^2 [6].

2.2 Operation of the Solar Simulator

The design of the solar simulator simplifies its operation. The molten salt vessel is centered about the lower aperture and the entire assembly is carefully lowered onto the vessel until the base of the simulator rests on the vessel insulation. The solar simulator in operation is illustrated in Figure (5) below:

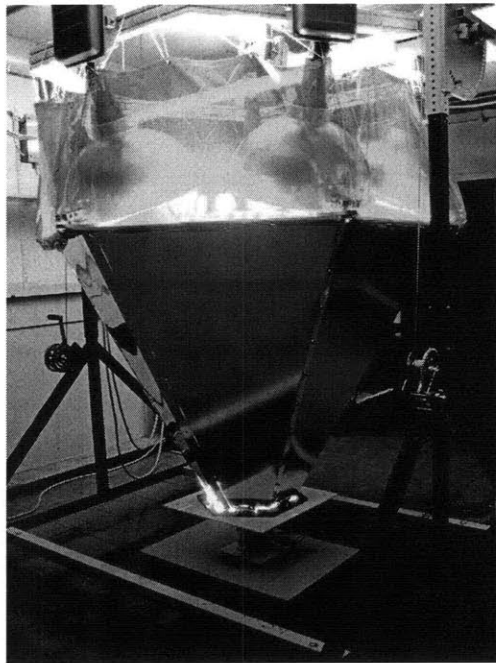


Figure 5: Solar simulator in with salt heat exchanger in operation. [14]

After the concentrator cone is in position, the simulator is powered on and the temperature at different positions across the molten salt receiver are recorded. After the end of each experiment the simulator is raised and secured in place and the salt receiver is moved away from the simulator and allowed to cool.

Chapter 3

Setup & Procedure

3.1 Experiment Design

3.1.1 Receiver Tank Geometry

The purpose of the experiment was to observe the thermal-fluids behavior as a function of time and position in the solar receiver. This was accomplished by recording the temperature distribution in the solar receiver as a function of time and the aspect ratio (See Section 3.2.1). As part of the validation process it was necessary to test the solar receiver system at different aspect ratios. A basic schematic of the solar receiver without the sensor setup, is illustrated in Figure (6) below:

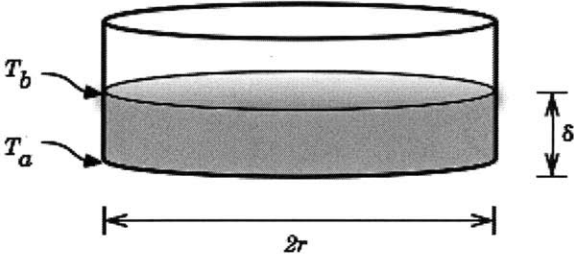


Figure 6: Schematic of the receiver tank geometry. The radius r and the molten salt depth δ defined. These parameters were used in defining the aspect ratio, and varied throughout each experiment (See Section 3.4.1).

A literature review [15-17] suggests that there is a strong correlation between the geometry of the fluid enclosure and the Rayleigh (Ra) number, which at a critical value Ra_c determines the transition from pure conductive heat transfer interaction to the development of axisymmetric convection currents.

3.2 Experimental Procedure

The experiment was designed to determine the dependence of the thermal-fluids behavior on the aspect ratio and to collect temperature data throughout the molten salt

receiver. The local temperature distribution and the dependence on the aspect ratio was based in the validation of the numerical thermal model and to obtain any available design information.

3.2.1 Sensor Setup

A K-type thermocouple array was used to capture the temperature behavior of the molten salt as a function of time. Considering the significance of the Rayleigh number to the onset of the convection regime, thermocouples were placed near the salt depths denoted T_b and T_a in Figure (6). These measurements were used to calculate the Rayleigh numbers that developed through the course of each experiment.

The thermocouple array included intermediate sensors to measure the temperature distribution in the axial direction of the solar receiver cylinder. The radial temperature distribution was measured by an array of thermocouples placed in a radial line at the bottom of the solar receiver. The entire thermocouple array is illustrated in Figure (7) below:

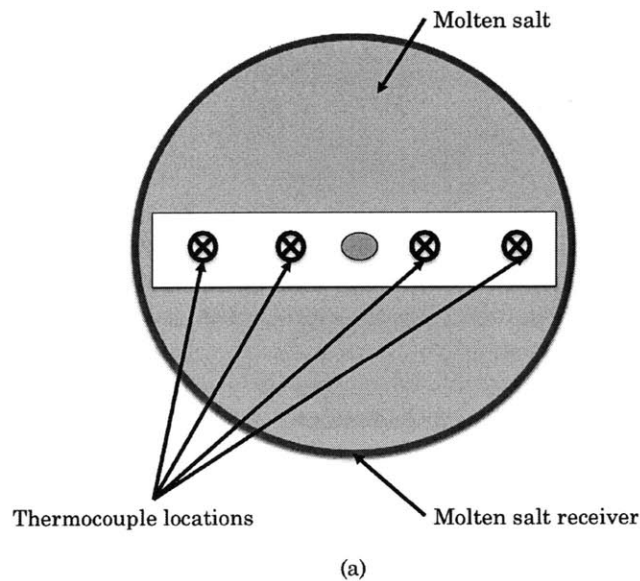


Figure 7a: Sensor setup. Top view (a); side view (b), with the relative position of the thermocouple sensors within the salt receiver vessel.

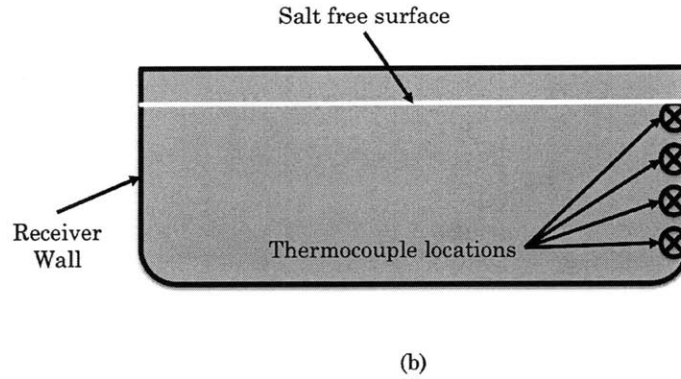


Figure 7b: Sensor setup. Top view (a); side view (b), with the relative position of the thermocouple sensors within the salt receiver vessel.

3.2.2 Experimental Protocol

Each experiment varied the aspect ratio, defined by Equation (14) below. The receiver tank was wrapped in ceramic and standard house fiberglass insulation around its circumference as illustrated by Figure (8) below. The tank was wrapped in insulation to minimize the heat flux in the radial direction and to approximate the adiabatic wall boundary conditions prescribed in the numerical simulations.

The experiments were carried out using Hitec Solar Salt. This salt mixture is composed of 60 wt%-40 wt% $\text{NaNO}_3\text{-KNO}_3$ [18]. The material properties of this binary salt mixture in its molten state are listed in Appendix C.

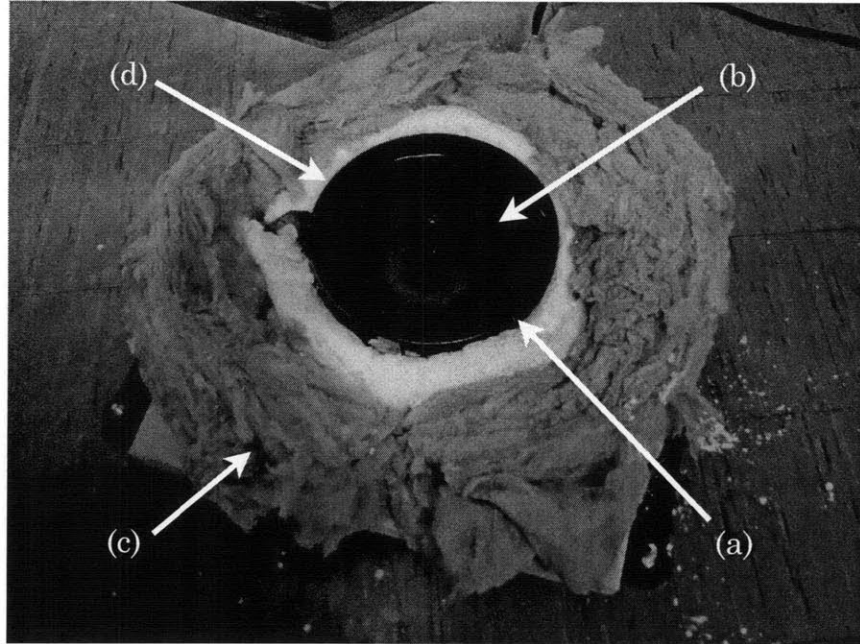


Figure 8. Salt receiver tank with insulation. The labels are as follows: (a) Molten salt receiver; (b) molten salt; (c) fiberglass insulation; (d) ceramic-based insulation.

The insulated receiver was placed under the simulator and aligned with the simulator aperture. The simulator was lowered until its bottom surface slightly compressed the thermal insulation and then it was secured in place. After all restraints and sensors were checked the stadium lights were switched on. The experiment was allowed to run for a span of about four hours, to allow the molten salt system to reach a steady-state temperature.

3.3 Simulation Parameters

The simulation code was run under a set of operating parameters only differing in the aspect ratio ϕ . Other parameters, such as the temperature-dependent density, the initial temperature, and other thermophysical properties remained the same across all simulations. A summary of the simulation parameters can be found in Table (2) below:

Table 2: Simulation parameters. These parameters were held constant through and in each simulation. The initial temperature value listed here is the average value for all experiments

Parameter	Value
Time step	$1.0 \cdot 10^{-2}$ s
Vessel side length (Equal area assumption)	0.2481 m
Gravity	9.789 m/s ²
Initial temperature	530.02 K
Specific heat capacity [18]	1550 J/(kg · K)
Thermal conductivity [18]	0.537 W/(m · K)
Average solar input [14]	45 kW/m ²

The simulation is able simulate a cuboid vessel. As a result, the dimensions of the simulated vessel geometry needed to be determined to have a point of comparison between the cylindrical experimental setup and the cubical simulation geometry. Thus, two options were explored: An equal area assumption and an inscribed circle assumption. For these simulations an equal area assumption was chosen to accurately model the energy input to the simulated receiver.

3.4 The Rayleigh Number

The Rayleigh number is a dimensionless quantity defined as the product of the Prandtl (Pr) and Grashof (Gr) numbers [3, 13]. The Rayleigh number can be interpreted as the ratio of the buoyancy forces in a variable-density medium to the thermal and momentum diffusivities in the same medium. The Rayleigh number is defined with Equation (13) below:

$$Ra = Pr \cdot Gr = \frac{g\beta}{\nu\alpha_D}(T_a - T_b)\delta^3 \quad (13).$$

Available research [15-17] suggest that the critical Rayleigh number is a function of the aspect ratio [16]. This relationship is discussed in Appendix D.

3.4.1 The Aspect Ratio

Because of its significant function in determining the onset of free convection, the aspect ratio was treated as the main independent variable in this set of experiments. Previous experience with the numerical model indicates a range of observed behaviors as the aspect ratio varies [2]. The aspect ratio is defined as the ratio of the molten salt depth to the diameter of the cylindrical receiver. This relationship is given by Equation (14) below:

$$\phi = \frac{\delta}{2r} \quad (14)$$

The experiments were done with aspect ratios near the proposed design dimensions [1] by Slocum ($\phi \approx 0.2$) and additionally explored the effect of changing aspect ratios below and above the proposed design values to explore the thermal-fluid behavior of the system.

Chapter 4

Experimental Results

4.1 Onset of Convection and the Rayleigh Number

Negative Rayleigh numbers are possible if a vertical cylinder is heated from above [19]. With the definition as given by Equation (13), the behavior of the Rayleigh number is given by the following relationship:

$$Ra > 0 \text{ if } T_a > T_b \tag{15a),}$$

$$Ra < 0 \text{ if } T_a < T_b \tag{15b).}$$

Thus we should expect that if the bottom temperature in the vessel is higher than that of the free salt surface that the Rayleigh number will be positive and viceversa. The critical Rayleigh numbers for the onset of convection according to the model in Appendix D are given in Table (3) below:

Table 3: Critical Rayleigh numbers for the tested aspect ratios.

Aspect Ratio, (ϕ)	Critical Rayleigh Number, (Ra_c)
0.100	5.7481×10^4
0.150	3.2214×10^4
0.179	2.3324×10^4
0.202	1.8082×10^4
0.214	1.5783×10^4
0.227	1.3824×10^4

The Rayleigh numbers were calculated using the mean central temperature at the

vessel bottom as T_a and the temperature immediately beneath the free salt surface as T_b (See Figure 6). The results of the calculations for each aspect ratio are illustrated in Figure (9) below:

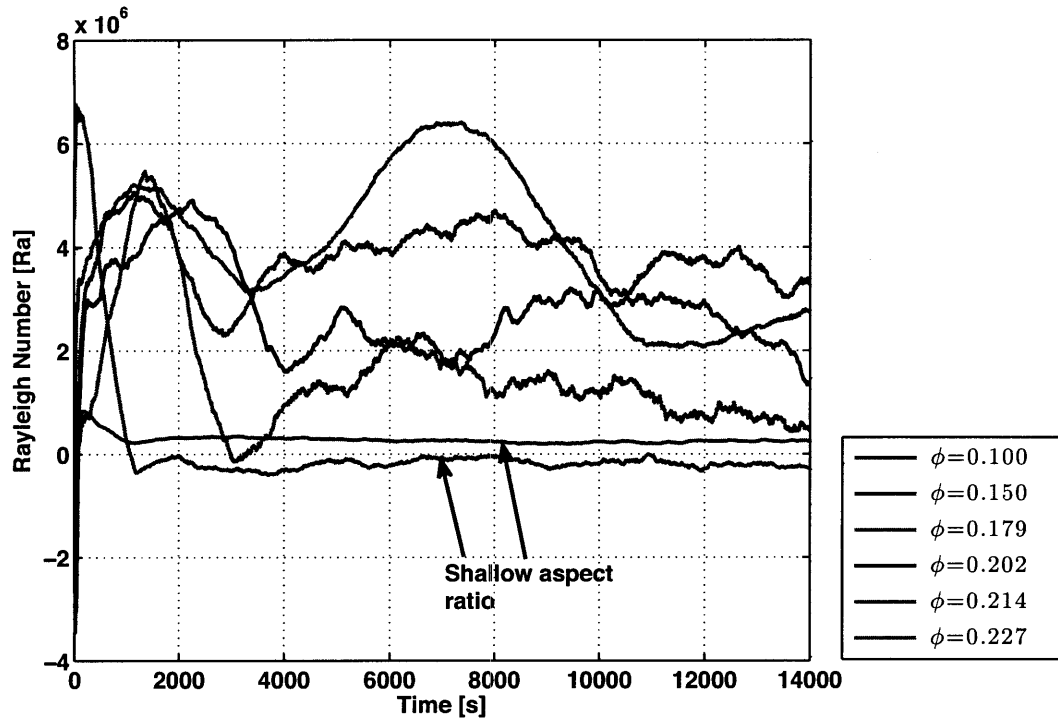


Figure 9: Experimental Rayleigh numbers. The experimental results indicate the possibility of a bifurcation in the molten salt thermal behavior as the aspect ratio decreases. For the shallow aspect ratios, the Rayleigh number stabilizes after an initial transient stage. As the aspect ratio increases the Rayleigh number oscillates for the duration of the experiment, but does not appear to follow other trend with respect to the aspect ratio. The code used to calculate the experimental Rayleigh number is given in Appendix E.

The percentage of the total time spent in the convective regime was calculated using the critical Rayleigh values from Table (3). The molten salt system is above the critical Rayleigh number for an average 99.12% of the total time for the experiment time. It is important to note that the experiment at $\phi=0.150$ spent 7.86% of the time in the convective regime then goes into a regime where the Rayleigh numbers are negative. This outlier result was not included in the averaging calculations.

4.2 Dimensionless Rise Time

The design of the solar receiver will benefit from the estimates of the temperature rise time as a function of the aspect ratio. Although the system cannot be modeled with a lumped thermal capacitance model (The Biot number for this system is about 0.67) the system dynamics follow an exponential temperature rise. The dynamics of the thermal system were modeled by Equation (16):

$$T(t) = a - be^{-\frac{t}{\tau}} \tag{16}.$$

The temperature rise time of each experiment was calculated from the experimental data and the non-dimensionalized using the Fourier number, as defined by Equation (17) below:

$$Fo = \frac{k\tau}{\rho(t = \tau)c_p\delta^2} \tag{17}.$$

The experimental data was fitted with an empirical model of the dependence of the dimensionless time on the aspect ratio. The results of this analysis are illustrated in Figure (10) below:

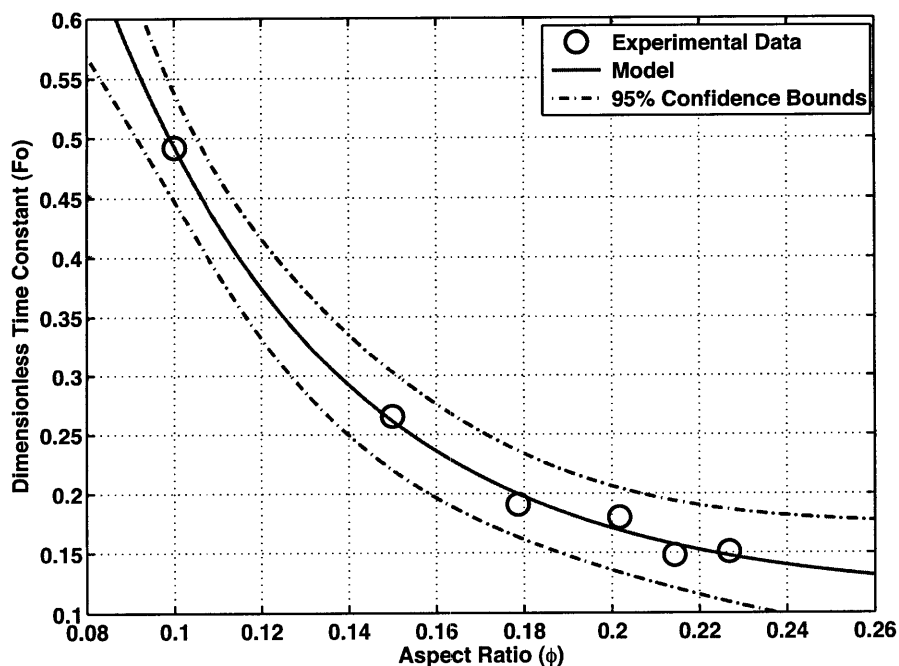


Figure 10. Dimensionless time constant as a function of aspect ratio. The dimensionless model has an average error of 3.41% over the collected data range. The temperature-dependent density was evaluated at $t=\tau$.

The dependence of the dimensionless time constant on the aspect ratio was fitted using MATLAB cftool utility and found and can be estimated with the empirical relationship expressed by Equation (17):

$$Fo(\phi) = 2.645e^{-18.69\phi} + 0.112 \quad (17).$$

This model was derived from empirical data and gives an average error of 3.41%, and has the potential to be useful in designing systems with a temperature rise time constraint.

4.3 Non-Dimensional Steady State Temperature

The average values for the top and bottom dimensionless temperature are dependent on the aspect ratio. The dimensionless temperature is defined, along with other dimensionless parameters, in Appendix B. The following is an analysis of the top and bottom average steady state temperatures as a function of the aspect ratio.

The average temperature was calculated for the bottom of the molten salt receiver. Using the non-dimensional temperature values, an empirical model was developed to estimate the relationship between the steady state temperature at the salt receiver bottom on the aspect ratio. The results of this analysis are illustrated in Figure (11) below:

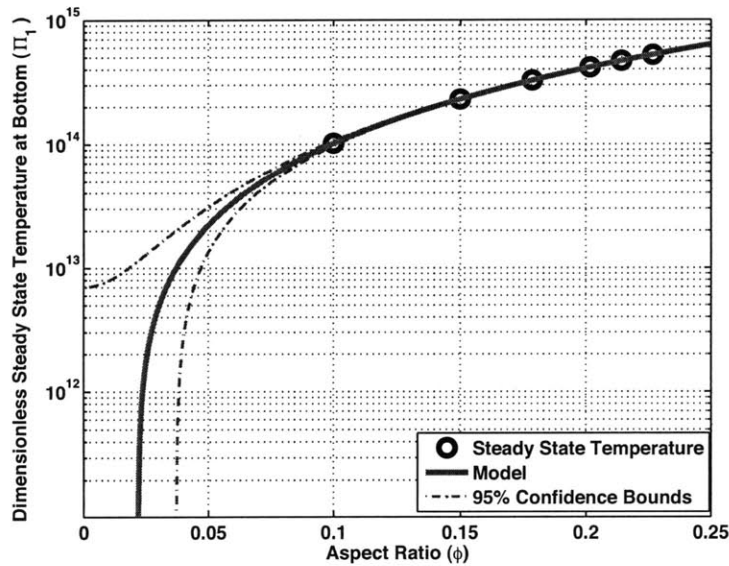


Figure 11: Dimensionless steady state temperature at vessel bottom.

The empirical model determined for the steady state temperature at the vessel bottom is given by Equation (18):

$$\Pi_1(\phi)_{bottom} = 9.532 \times 10^{15} \phi^{1.949} - 5.509 \times 10^{12} \quad (18)$$

The same analysis was carried out on the steady state temperature near free boundary. The results for the dimensionless steady state temperature at the salt free surface is illustrated by Figure (12) below:

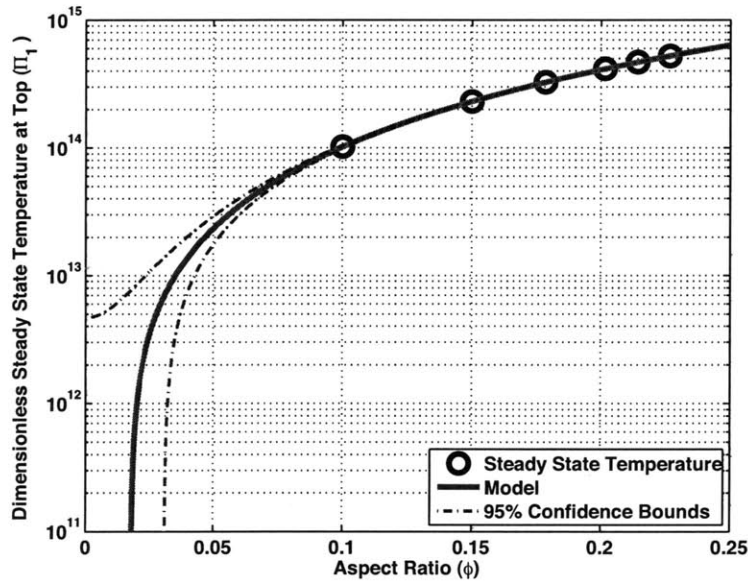


Figure 12: Dimensionless steady state temperature at the salt free surface.

The empirical model for the dimensionless steady state temperature at the salt free surface is given by Equation (19) below:

$$\Pi_1(\phi)_{top} = 9.794 \times 10^{15} \phi^{1.968} - 3.52 \times 10^{12} \quad (19)$$

The models represented by Equations (18, 19) are limited to aspect ratios greater than 0.1. The dependence of the steady-state temperature on other parameters, such as the incoming heat flux should be explored. The validity of these models should also be explored to determine the applicability of the models presented in Equations (17-18).

Chapter 5

Simulation Results

5.1 Temperature Rise Dynamics

Each simulation was allowed to run for an average of 1300 simulation seconds. However, it became apparent that the system surpassed the experimental temperatures in a very short time spans (This occurrence is discussed in Section 6.1.1). The average bottom temperatures for all the simulated experiments are illustrated in Figure (13) below:

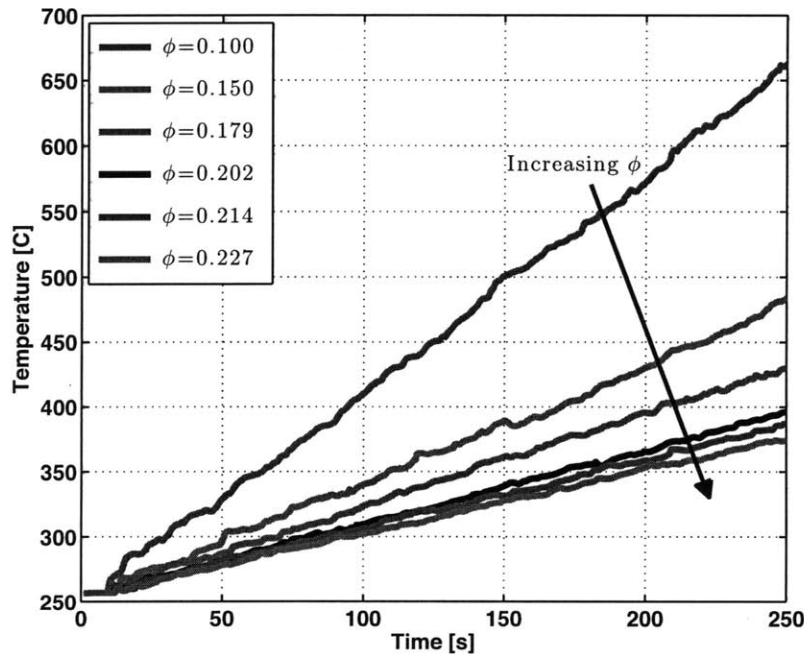


Figure 13: Time history of the mean vessel bottom temperature. The temperature traces do not follow an expected exponential-type rise. Instead, they rise with a nearly-linear profile. However, as the aspect ratio increases, the slope of the temperature decreases, as is expected since the thermal mass of the system increases with the aspect ratio.

5.2 Identification of Convective Behavior

One of the main aspects of the simulation was to model the convective behavior of the molten salt system at operating temperatures. Convection begins to occur when

Rayleigh-Taylor (RT) instabilities begin to appear, at the time when the system reaches its critical Rayleigh number [20, 21]. These type of instabilities are often called “fingers” because of their long and narrow shape. They form when a lower-density fluid pushes against a higher-density fluid [20]. These instabilities appear in all simulations. A typical scenario is illustrated in Figure (14) below:

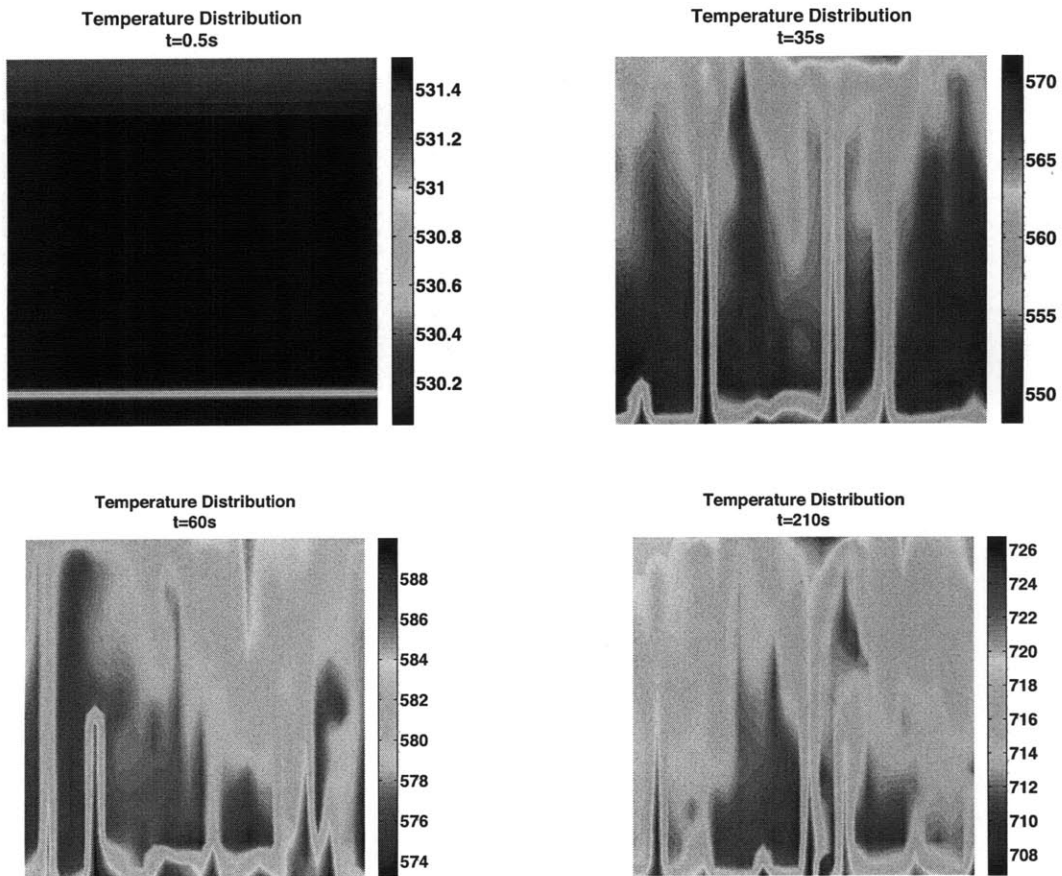


Figure 14: Cross-section of the simulated time evolution with aspect ratio $\phi = 0.150$. Rayleigh-Taylor instabilities formed by hotter fluid form at the vessel bottom. The instabilities then rise as a consequence of their lower density. Please note that all temperatures given are in Kelvin.

These structures do not only appear at one section of the vessel bottom, they appear throughout, taking time to become fully developed. The system begins with a mostly stratified temperature distribution and once the instabilities begin to form the simulation indicates the fluid begins to move along its central axis and then begin to descend near the walls.

The structures become well-developed with time, eventually occurring in the majority of the vessel bottom area. As the temperature increases, these structures begin to become symmetric. Other studies [15-17, 21] have confirmed that this appears in experiment and in similar simulations. The RT phenomena as a function of time is illustrated by Figure (15) below:

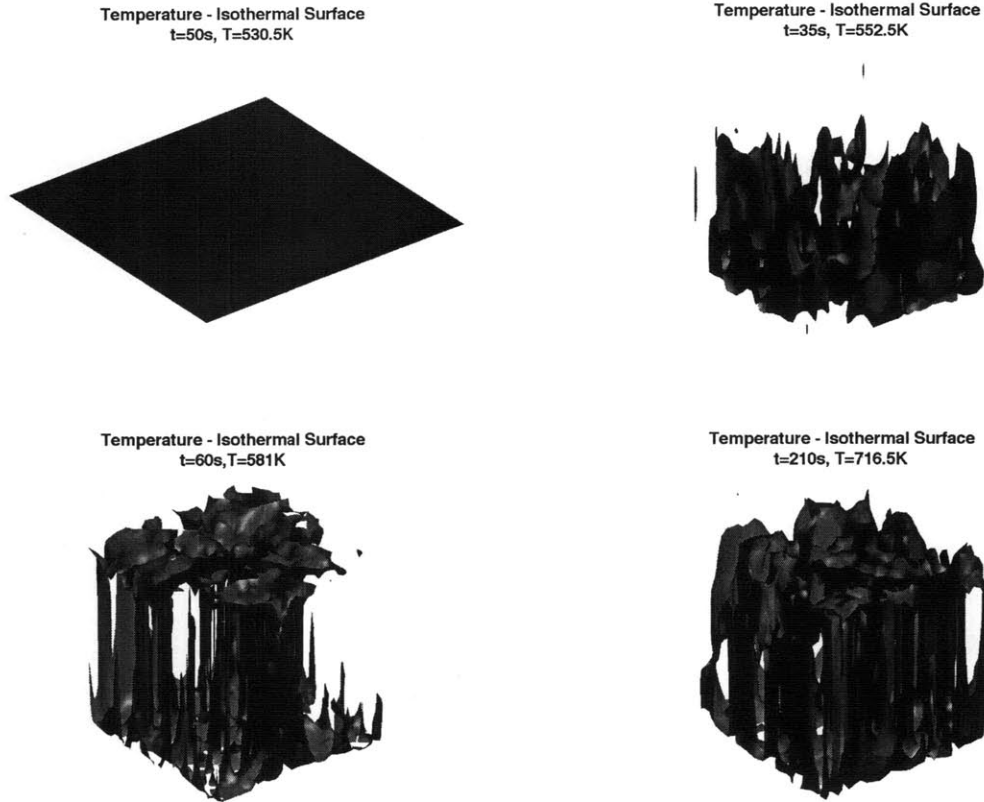


Figure 15: Simulated three-dimensional isothermal surfaces with aspect ratio $\phi = 0.150$. The fluid begins as a nearly isothermal medium. With time, Rayleigh-Taylor instabilities begin to form throughout the vessel area, becoming fully developed, indicating an active convective system as the system reaches higher Rayleigh numbers.

5.3 The Rayleigh Number in the Simulations

Another point of comparison is the Rayleigh numbers developed during the numerical simulations. The simulation Rayleigh numbers were calculated using Equation (13). The results of this analysis are illustrated by Figure (16) below:

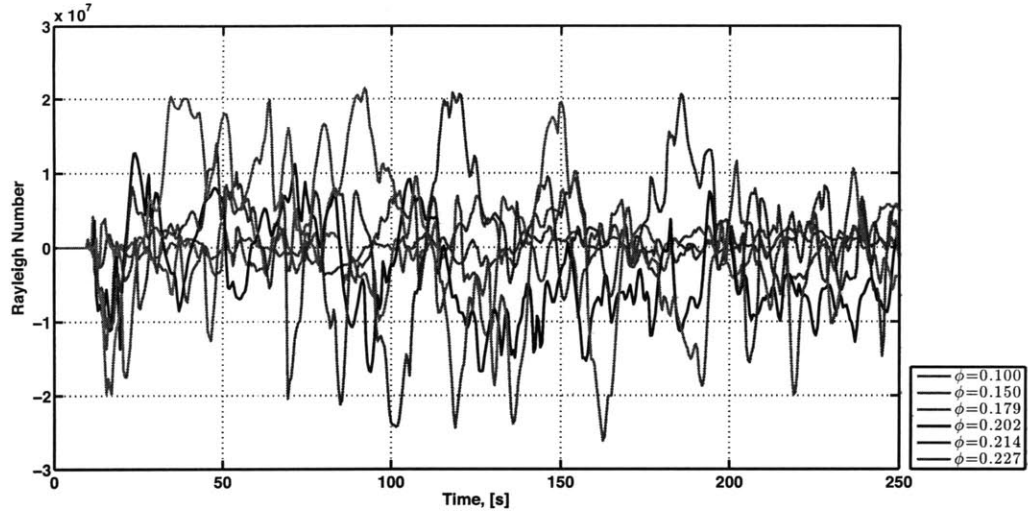


Figure 16. Rayleigh numbers in the numerical simulation. The simulations are above the critical Rayleigh number for about 49.53% of their run times.

The Rayleigh numbers in this simulation have an average value of zero throughout the simulations. However the Rayleigh numbers are within the same order of magnitude as those observed in the simulation. When compared to the experimental Rayleigh numbers, the simulation follows the same oscillatory behavior. The addition of the heat loss terms as recommended in Appendix F should allow the simulation to exhibit the same type of steady state behavior as the Rayleigh numbers observed in the experiments.

Chapter 6

Discussion & Conclusions

Although the numerical simulation captures the phenomena of the RT instabilities, it does not capture the steady-state temperature behavior observed in the experiments. Additionally, its temperature rise across all aspect ratios is much greater than that observed in the experiments. There are several immediate causes for this: the adiabatic boundary assumptions and the error in the absorption coefficient and the assumption of constant thermophysical properties.

6.1 Validity of the Boundary Condition Assumptions

6.1.1 The adiabatic free-surface assumption

Although an adiabatic free surface may simplify the numerical solving problem, it does not allow the simulated salt system to reach a steady state. Considering that the molten system includes only adiabatic boundaries, it should not experience any thermal losses, thus the molten salt system only stores thermal energy. This results in the linear temperature rise as observed in Section 5.1. An analysis of the thermal loss terms for this system is given in Appendix F. The author recommends that these thermal losses are incorporated into the model to describe the dynamics of the temperature rise. These changes will allow the simulation to approximate the characteristic dynamics of the temperature rise as observed in the experiments.

6.1.2 Geometric assumptions

The cuboid geometry captures the general convection behavior, however, other works [15-17, 21] have shown that to capture the characteristic behavior, the geometry must be the same. Thus, it is recommended that the boundary conditions be changed to a cylindrical configuration if the normal modes and the complete convective behavior are to be captured in the numerical simulation.

6.2 Validity of the Material Property Assumptions

6.2.1 Optical Absorbance Model

During the analysis of the optical absorbance data the author was advised that the data was most reliable for incident light with a wavelength ranging from 400 to 800 nm [11]. However, the solar models developed by NREL are comprised of spectral data ranging from nearly 0 to 4000 nm. At higher wavelengths, the absorption coefficient has been shown [11] to increase dramatically. More reliable measurements at higher wavelengths are necessary to capture the entire range of interactions between the incident long wavelength light and the molten salt medium, especially for the solar input at longer wavelengths.

6.2.2 Constant Thermophysical Properties

The issue of constant thermophysical properties is crucial to the convection problem, as the calculation of the Rayleigh number is highly sensitive to changing thermophysical properties. A review of the relevant and available literature only yielded the Boussinesq approximation for the mass density of the molten salts for the applicable temperature ranges. Extensive research did not find any other temperature-dependent models for other thermophysical properties. Once other models for the thermophysical properties of salts are determined, a more accurate numerical simulation should arise from the implementation of these thermophysical relations.

6.2.3 Optical System Assumptions

The simulation assumes that the incoming beam is completely absorbed by the molten salt. However, this assumption has not been experimentally verified. Another aspect of the optical system is that all the energy contained in the incoming is absorbed by the thermal system. Further studies on the optical interactions of the system considered should be done to fully characterize the physics of the incoming beam of light. This will allow the next iteration of the simulation code to be accurately model all the interactions between the incoming light beam and the molten salt.

6.3 Conclusion

Although this simulation exhibits is capable of reproducing the RT instabilities as expected during the onset of free convection, it is not capable of simulating the steady-state temperature behavior observed in experiment. An estimate of the convective losses over the free salt surface was recommended, however, the convective losses only account for an mean loss of about 2% of the thermal energy in the incoming solar beam. This leads the author to believe that there are other losses through conduction at the side walls that are not accounted for in the simulation. However, considering the large surface area of the vessel bottom and the lack of significant insulation at that location might be a source of significant source of thermal losses.

The most pressing recommendation thus becomes the integration of the thermal losses into the system. These are listed in Appendix F. The next step is to develop an improved model of the optical interactions between the incoming solar beam and the molten salt medium. The next concern would be to modify the simulation to be used with different receiver geometries and the surface properties of the vessel. Because the model already displays convective behavior, the full integration of all temperature-dependent quantities should be the last concern. This is supported by other investigations, in which the Boussinesq approximation for density suffices to obtain an accurate model of the thermal convection in the cylindrical vessel [15-17, 21].

With these recommended changes, the numerical simulation should represent an accurate model of the convective behavior and the interactions between the incoming solar beam and the molten salt.

Bibliography

- [1] A. H. Slocum, "Concentrated Solar Power on Demand," Massachusetts Institute of Technology, Cambridge, MA 2010.
- [2] J.-C. Nave, "Direct Numerical Simulation of the Coupled Optical/Thermal/Fluid Pond System," Massachusetts Institute of Technology, Cambridge, MA, 2009
- [3] F. P. Incropera and D. P. Dewitt, *Fundamentals of Heat and Mass Transfer*, 5th ed. New York: John Wiley & Sons, 2001.
- [4] G. J. Janz, *Thermodynamic and Transport Properties for Molten Salts: Correlated Equations for Critically Evaluated Density, Surface Tension, Electrical Conductance, and Viscosity Data* vol. 17: Springer Verlag, 1988.
- [5] John H. Lienhard IV and J. H. L. V, *A Heat Transfer Textbook*, 3rd ed. Cambridge, MA: Phlogiston Press, 2008.
- [6] K. Emery and D. Myers. (4/17/2010). *Reference Solar Spectral Irradiance: Air Mass 1.5*. Available: <http://rredc.nrel.gov/solar/spectra/am1.5/>
- [7] S. A. Kalogirou, *Solar Energy Engineering - Processes and Systems*. Burlington, MA: Elsevier, 2009.
- [8] NREL. (4/22/2010). *RReDC Glossary of Solar Radiation Resource Terms*. Available: <http://rredc.nrel.gov/solar/glossary/>
- [9] NASA. (2010, (4/22/2010)). *Water Vapor : Global Maps*. Available: http://earthobservatory.nasa.gov/GlobalMaps/view.php?d1=MYDAL2_M_SKY_WV#
- [10] J. Houghton, *The Physics of Atmospheres*, 3rd ed.: Cambridge University Press, 2001.
- [11] S. Passerini, "Summary of the Experimental Activity Focused on the Characterization of the Light Attenuation of Molten Salt (Nitrate and Chloride) Mixtures," Massachusetts Institute of Technology, Cambridge 2010.
- [12] A. J. Chorin, "Numerical Solution of the Navier-Stokes Equations," *Mathematics of Computation*, vol. 22, pp. 745-762, 1968.
- [13] S. S. Kutateladze and V. M. Borishanskii, *A Concise Encyclopedia of Heat Transfer*, 1st ed. New York: Pergammon Press, 1966.
- [14] D. Codd, *et al.*, "A Low-Cost High Flux Solar Simulator," pp. 1-15, 2010.
- [15] R. L. Frederick and F. Quiroz, "On the transition from conduction to convection regime in a cubical enclosure with a partially heated wall," *International Journal of Heat and Mass Transfer*, vol. 44, pp. 1699-1709, 2001.
- [16] K. Stork and U. Müller, "Convection in boxes: an experimental investigation in vertical cylinders and annuli," *Journal of Fluid Mechanics*, vol. 71, pp. 231-240, 1974.
- [17] G. Neumann, "Three-dimensional numerical simulation of buoyancy-driven convection in vertical cylinders heated from below," *Journal of Fluid Mechanics*, vol. 214, pp. 559-578, 1990.
- [18] "Hitec Solar Salt: Product Information," L. Coastal Chemical Co., Ed., ed. Houston.
- [19] G. Muller, *et al.*, "A two-Rayleigh-number model of buoyancy-driven convection in vertical melt growth configurations," *Journal of Crystal Growth*, vol. 84, pp. 36-49, 1987.
- [20] D. H. Sharp, "An Overview of Rayleigh-Taylor Instability," *Physica D*, vol. 12, pp. 3-18, 1984.
- [21] G. Müller, *et al.*, "A two-Rayleigh-number model of buoyancy-driven convection in vertical melt growth configurations," *Journal of Crystal Growth*, vol. 84, pp. 36-49, 1987.
- [22] L. M. Jiji, *Heat Convection*. Berlin: Springer Berlin Heidelberg, 2007.

Appendix A

Estimating the Volumetric Heat Generation

A Mathcad document was created to estimate the functional forms of the volumetric heat generation models from the solar spectrum data and the material properties of the $\text{KNO}_3\text{-NaNO}_3$ salt mixture. These were necessary because the computer simulations were designed to take in a functional form of the volumetric heat generation as a function of tank depth, as defined in Equation (6).

The functional forms of the volumetric heat generation were estimated with sum of two exponential terms using Matlab's cftool curve-fitting utility. The exponential fits have the form:

$$q(z) = ae^{bz} + ce^{dz} \quad (19)$$

The results of the curve fitting analysis are tabulated below, along with their corresponding units.

Table 4: Fit constants for the volumetric heat generation model

Spectrum	a , [$\text{W} \cdot \text{m}^{-3}$]	b , [m^{-1}]	c , [$\text{W} \cdot \text{m}^{-3}$]	d , [m^{-1}]
Planck model	$1.562 \cdot 10^7$	-552.3	$2.926 \cdot 10^4$	-0.9324
Extraterrestrial	$1.455 \cdot 10^7$	-540.4	$3.218 \cdot 10^4$	-1.025
Global tilt	$1.998 \cdot 10^6$	-357.1	$3.607 \cdot 10^4$	-1.049
Direct+circumsolar	$1.280 \cdot 10^6$	-331.2	$3.540 \cdot 10^4$	-1.018

The reflected heat at the surface is represented by Equation (20):

$$q_{ref} = q_{in} - \int_0^{\delta} q(z) dz = q_{in} - \left[\frac{a}{b}(e^{b\delta} - 1) + \frac{c}{d}(e^{d\delta} - 1) \right] \quad (20)$$

Appendix B

Buckingham Pi Theory Analysis

Temperature

$$\Pi_1 = \frac{T\delta^2\rho^2k}{\mu^3}$$

Time, but can also correspond to the Fourier number

$$\Pi_2 = \frac{t\mu}{\delta^2\rho} \quad Fo = \frac{kt}{\rho c_p \delta^2}$$

Gravity, leads to the Grashof number

$$\Pi_3 = \frac{g\delta^3\rho^2}{\mu^2} = \frac{Gr}{\beta\Delta T}$$

Pressure

$$\Pi_4 = \frac{P\delta^2\rho}{\mu^2}$$

Vessel Radius

$$\Pi_5 = \frac{r}{\delta}$$

Incoming wavelength

$$\Pi_6 = \frac{\lambda}{\delta}$$

Specific heat capacity, leads to the Prandtl number

$$\Pi_7 = \frac{c_p\mu}{k} = Pr$$

Absorption

$$\Pi_8 = \alpha\delta$$

Volumetric heat transfer

$$\Pi_9 = \frac{q\delta^4\rho^2}{\mu^3}$$

Fluid velocity, leads to the Reynolds number

$$\Pi_{10} = \frac{u\delta\rho}{\mu} = Re$$

Thermal expansion coefficient

$$\Pi_{11} = \frac{\beta\mu^3}{\delta^2k\rho^2}$$

Solar constant

$$\Pi_{12} = \frac{q_{beam}\delta^3\rho^2}{\mu^3}$$

Light intensity

$$\Pi_{13} = \frac{I\delta^4\rho^2}{\mu^3}$$

Convective heat transfer coefficient, leads to the Nusselt Number

$$\Pi_{14} = \frac{h_c\delta}{k} = Nu$$

Appendix C

Material & Optical Properties for $\text{KNO}_3\text{-NaNO}_3$ Mixtures

The experiments used a 40%wt KNO_3 60%wt NaNO_3 salt mixture, commercially known as Hitec Solar Salt. The empirical constitutive relation as published by Janz were used to interpolate a value for the actual salt composition corresponds to 36 %mol-64 %mol KNO_3 NaNO_3 mixture, since the values are only tabulated in mol% form. The interpolated relationship is given by Equation (21) below:

$$\rho(T) = 2.2874 - 6.6692 \times 10^{-4}T \quad (21)$$

where the density is given in units of $\text{g} \cdot \text{cm}^{-3}$ and T is the absolute temperature in Kelvins.

Subsequent iterations of the numerical simulations should consider the temperature-dependent behavior in attempt to capture a more accurate model of the thermal-fluids behavior of the molten salt system. The material property data available only lent itself to a line-fitting analysis for the molten salt density.

The following data were given by the manufacturer for the Hitec Solar salt in its molten state [18] :

Table 5: Manufacturer data for the Hitec Solar Salt mixture.

Property	Value	Units
Specific Heat	1550	$\text{J} \cdot (\text{kg}^{-1}\text{K}^{-1})$
Density	1794	$\text{kg} \cdot \text{m}^{-3}$
Dynamic Viscosity	0.002	$\text{Pa} \cdot \text{s}$
Thermal Conductivity	0.537	$\text{W} \cdot (\text{m}^{-1}\text{K}^{-1})$

The following optical data were collected by Passerini. They correspond to the salt attenuation data for range molten salt temperatures [11]. The data provided was deemed

reliable by Passerini from a range of 400 nm to 800 nm [11]. Only this data in this range was used to fit lines to the data. The fit lines are characterized by Equation (22):

$$\alpha(\lambda) = ae^{b\lambda} + ce^{d\lambda} \quad (22).$$

The fit constants for light attenuation as a function of temperature are given in Table (6) below:

Table 6. Fit constants for the light attenuation coefficient. The given fits take in wavelength in nanometers and output the attenuation in units of cm^{-1} . The fit attenuation coefficients for the temperatures listed are illustrated below for their valid wavelength range (400-800 nm).

Temperature [C]	a , [cm^{-1}]	b , [nm^{-1}]	c , [cm^{-1}]	d , [nm^{-1}]
250	$2.774 \cdot 10^{11}$	-0.07104	0.04269	-0.001977
300	$3.822 \cdot 10^{11}$	-0.07122	0.04702	-0.002114
350	$3.15 \cdot 10^{11}$	-0.07003	0.06573	-0.002606
400	$3.044 \cdot 10^{11}$	-0.06980	0.04336	-0.001962

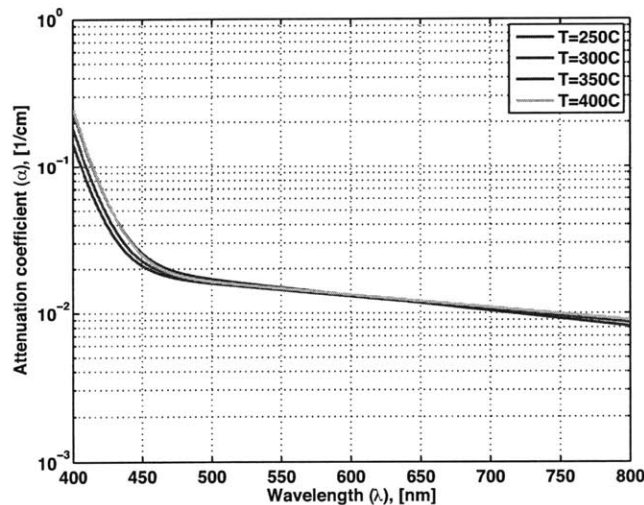


Figure 17: Light attenuation coefficient in the wavelength absorption range [11].

Appendix D

The Critical Rayleigh Number

The critical Rayleigh number for convection in a cylindrical vessel was experimentally determined for a range of aspect ratios [16, 21]. The empirical data was fitted with a curve using MATLAB's cftool utility, and is given by Equation (23) below:

$$Ra(\phi) = 1.867 \times 10^5 e^{-12.1\phi} + 1842e^{-0.02154\phi} \quad (23).$$

The data, along with the model given by Equation (23) is presented in Figure (18) below:

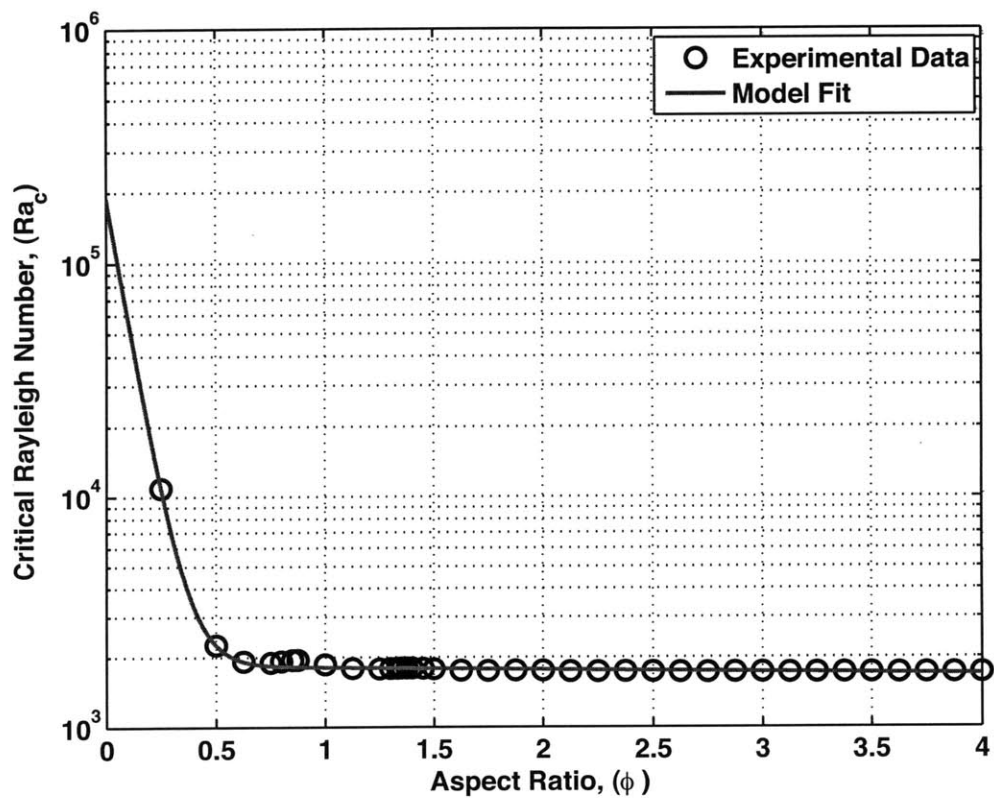


Figure 18: Graphical form of the critical Rayleigh number for cylindrical geometry.

Appendix E

Matlab Code

```
%Rayleigh number calculator
%Juan Fernando Rodríguez Alvarado, (MIT)

%This function takes in an experimental data vector and calculates the
%Rayleigh number of the molten salt system.
%function ra=rayleigh(data,depth,TopSensor) takes in a temperature vector
%data, the depth of the fluid, and the column or row number in which the
%topmost temperature sensor is placed (Usually immediately below the free
%fluid surface).

function ra=rayleigh(data,depth,TopSensor)

%-----Pre-allocations-----%

p=zeros(length(data),1); %% Density vector prealloc.
v=zeros(length(data),1); %% Kinematic viscosity prealloc.
ra=zeros(length(data),1); %% Rayleigh number prealloc.
a=zeros(length(data),1); %% Thermal diffusivity prealloc

%-----Set Environmental Variables-----%

g=9.78932; %% Gravitational acceleration [m/s]
B=3.633e-4; %% Coefficient of volumetric thermal expansion [1/K]
u=0.0021; %% Kinematic viscosity [Pa*s]
k=0.537; %% Thermal conductivity [J/(m*K)]
cp=1550; %% Specific thermal capacity [J/(kg*K)]
To=273.16; %% 0 deg C in Kelvin

%-----Data Processing-----%
```

```

time=data(:,1); %% Time vector definition
TempTop=data(:,TopSensor); %% Top temperature data definition
TempRange=data(:,3:4); %% Extracts temp. at center bottom of vessel
TempBot=mean(TempRange,2); %% Bottom temperature average;
Temp=(TempTop+TempBot+2*To)/2; %% Bottom temp. to calculate
density (absolute temperature)

%-----Rayleigh Number Calcs-----%

for i=1:length(data);
    p(i)=1000*(2.2874-6.6692e-4*Temp(i)); %% Molten Salt Density [kg/m^3]
    v(i)=u/p(i); %% Dynamic viscosity [m^2/s]
    a(i)=k/(p(i)*cp); %% Thermal diffusivity [m^2/s]

    %Rayleigh number-----%

    ra(i)=g*B/(v(i)*a(i))*(TempBot(i)-TempTop(i))*depth^3;

end;

```

Appendix F

Thermal Losses

The current simulation does not take into account thermal losses due to interactions of the solar receiver with the environment. The following is an initial thermal analysis that will allow for modification of the code in future validations. The total thermal loss to the environment can be written as Equation (24):

$$Q_{tot} = \sum Q_{out} = Q_{out}^{cond} + Q_{out}^{bot} + Q_{out}^{conv} \tag{24}.$$

To account for the thermal losses in the radial direction, we consider the system illustrated by Figure (19) below:

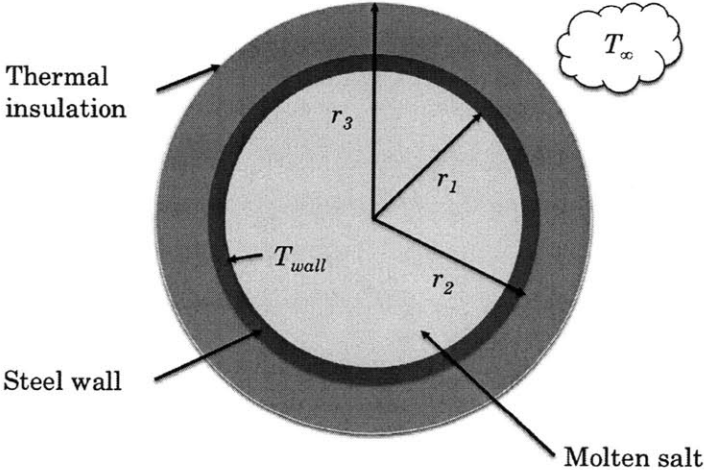


Figure 19: Solar receiver geometry for thermal losses in the radial direction.

Assuming that the steel wall and the thermal insulation have thermal conduction coefficients k_{steel} and k_{ins} , respectively, we can write their effective thermal resistance as:

$$R_{eff} = \frac{\ln\left(\frac{r_2}{r_1}\right)}{2\pi L k_{steel}} + \frac{\ln\left(\frac{r_3}{r_2}\right)}{2\pi L k_{ins}} \quad (25).$$

The heat transfer through the combined steel-insulation is defined as:

$$Q_{out}^{cond} = \frac{T_{wall} - T_{\infty}}{R_{eff}} = UA(T_{wall} - T_{\infty}) \quad (26a),$$

$$U = \frac{1}{\frac{r_1}{k_{steel}} \ln\left(\frac{r_2}{r_1}\right) + \frac{r_1}{k_{ins}} \ln\left(\frac{r_3}{r_2}\right)} \quad (26b).$$

The area A considered for the analysis will be the outer surface area of the steel tank. For the chosen area, the radial heat losses are expressed by Equation (27) below:

$$Q_{out}^{cond} = \frac{2\pi r_1 L}{\frac{r_1}{k_{steel}} \ln\left(\frac{r_2}{r_1}\right) + \frac{r_1}{k_{ins}} \ln\left(\frac{r_3}{r_2}\right)} (T_{wall} - T_{\infty}) \quad (27).$$

The thermal losses through the solar receiver bottom can be considered as a heat conduction through the steel bottom, with thickness t_{steel} . The conduction heat transfer through the salt receiver bottom is expressed by Equation (28):

$$Q_{loss}^{bot} = \frac{k_{steel} A_{bot}}{t_{steel}} (\bar{T}_{bot} - T_{\infty}) \quad (28).$$

The thermal losses from natural convection due to the air circulation above the molten salt surface are given by Equation (29):

$$Q_{loss}^{conv} = h_c A_{salt} (\bar{T}_{surf} - T_{\infty}) \quad (29).$$

Several relationships exist for determining the free convection coefficient for this system. One that is commonly found in literature [3, 22] is given by Equation (30) below:

$$Nu = \frac{h_c L_c}{k_{air}} = 0.54(Ra)^{1/4} \quad (30),$$

where the Rayleigh number for free convection above the salt surface is given by Equation (31):

$$Ra = g \left(\frac{\beta}{\nu \alpha} \right)_{air} (T_{surf} - T_{air}) L_c^3 \quad (31).$$

The thermophysical properties of air, except for the coefficient of volumetric expansion, are calculated at the film temperature defined by Equation (32):

$$T_{film} = \frac{T_{air} + T_{surf}}{2} \quad (32).$$

For an ideal gas, the coefficient of thermal expansion can be approximated as the inverse of the absolute temperature of the air. This relationship is given by Equation (33):

$$\beta = \frac{1}{T_{air}} \quad (33).$$

The characteristic length for this system is defined as the ratio of the exposed salt surface area to the perimeter enclosing the salt vessel, thus it is expressed as Equation (34):

$$L_c = \frac{A_{salt}}{\wp} \quad (34).$$

For the experimental conditions encountered in this study, the convection coefficient was found to have a mean value of $7.23 \text{ W} \cdot \text{m}^{-2}\text{K}^{-1}$. For these values, the mean energy loss due to free convection is 50 W.